

ARTICLE



<https://doi.org/10.1038/s41467-022-29495-y>

OPEN

# Data-driven discovery of high performance layered van der Waals piezoelectric NbOI<sub>2</sub>

Yaze Wu<sup>1,2,9,10</sup>, Ibrahim Abdelwahab<sup>1,2,3,10</sup>, Ki Chang Kwon<sup>1,3</sup>, Ivan Verzhbitskiy<sup>1,2</sup>, Lin Wang<sup>1,3</sup>, Weng Heng Liew<sup>4</sup>, Kui Yao<sup>1,4</sup>, Goki Eda<sup>1,2</sup>, Kian Ping Loh<sup>1,2,3,5</sup>✉, Lei Shen<sup>1,6,7</sup>✉ & Su Ying Quek<sup>1,2,5,8</sup>

Using high-throughput first-principles calculations to search for layered van der Waals materials with the largest piezoelectric stress coefficients, we discover NbOI<sub>2</sub> to be the one among 2940 monolayers screened. The piezoelectric performance of NbOI<sub>2</sub> is independent of thickness, and its electromechanical coupling factor of near unity is a hallmark of optimal interconversion between electrical and mechanical energy. Laser scanning vibrometer studies on bulk and few-layer NbOI<sub>2</sub> crystals verify their huge piezoelectric responses, which exceed internal references such as In<sub>2</sub>Se<sub>3</sub> and CulnP<sub>2</sub>S<sub>6</sub>. Furthermore, we provide insights into the atomic origins of anti-correlated piezoelectric and ferroelectric responses in NbOX<sub>2</sub> (X = Cl, Br, I), based on bond covalency and structural distortions in these materials. Our discovery that NbOI<sub>2</sub> has the largest piezoelectric stress coefficients among 2D materials calls for the development of NbOI<sub>2</sub>-based flexible nanoscale piezoelectric devices.

<sup>1</sup> Department of Physics, National University of Singapore, Singapore, Singapore. <sup>2</sup> Centre for Advanced 2D Materials and Graphene Research Centre, Singapore, Singapore. <sup>3</sup> Department of Chemistry, National University of Singapore, Singapore, Singapore. <sup>4</sup> Institute of Materials Research and Engineering, Agency for Science, Technology and Research (A\*STAR), Singapore, Singapore. <sup>5</sup> NUS Graduate School, Integrative Sciences and Engineering Programme, National University of Singapore, Singapore, Singapore. <sup>6</sup> Department of Mechanical Engineering, National University of Singapore, Singapore, Singapore. <sup>7</sup> Engineering Science Programme, National University of Singapore, Singapore, Singapore. <sup>8</sup> Department of Materials Science and Engineering, National University of Singapore, Singapore, Singapore. <sup>9</sup> Present address: Institute of High Performance Computing, Agency for Science, Technology and Research (A\*STAR), Singapore, Singapore. <sup>10</sup>These authors contributed equally: Yaze Wu, Ibrahim Abdelwahab. ✉email: [chmlohkp@nus.edu.sg](mailto:chmlohkp@nus.edu.sg); [shenlei@nus.edu.sg](mailto:shenlei@nus.edu.sg); [phyqsy@nus.edu.sg](mailto:phyqsy@nus.edu.sg)

Piezoelectric materials enable the interconversion between mechanical and electrical energy. This is made possible by the change in polarization of the material when it is stretched or compressed. As such, piezoelectric materials are integral components of intelligent, multi-functional devices and drive a multi-billion dollar industry<sup>1</sup> through their applications as sensors, actuators, energy harvesters, etc.<sup>2–7</sup>. The recent thrust toward flexible nanoscale devices creates a need for two-dimensional (2D) piezoelectric materials. Piezoelectric materials comprised of one or few layers of layered van der Waals (vdW) systems are particularly useful for increasingly important niche applications such as actuators with extreme atomic-scale precision<sup>8</sup> as well as wearable sensors and smart material applications that require a large voltage signal in response to a small amount of physical deformation. 2D piezoelectric materials provide a practical alternative to micro-scale battery packs, functioning as nano-generators to power nanoscale devices<sup>9</sup>.

Thus far, the discovery of 2D piezoelectric materials has mostly been ad hoc, for example, by performing calculations on specific 2D materials that are known to be ferroelectric. However, with an ad hoc approach, it is difficult to ascertain if the 2D material indeed has optimal piezoelectric coefficients. Experimentally, it is also challenging to quantitatively compare the piezoelectric coefficients of 2D materials<sup>10</sup>. The objective of this work is to perform a systematic high throughput search through a 2D material database, in order to rank the 2D materials according to the size of their intrinsic piezoelectric coefficients. While 2D materials down to nanometers in thickness are sufficient for flexible nanoscale devices, symmetry-breaking in the monolayer can lead to the emergence of piezoelectricity in the monolayer even when the parent bulk materials are not piezoelectric<sup>11</sup>. Thus, we focus our search on monolayers. Out of 109 piezoelectric monolayers that we identify, the family of niobium oxydihalides NbOX<sub>2</sub> (X = Cl, Br, I) is predicted to have among the largest in-plane piezoelectric stress coefficients, an order of magnitude larger than those of most reported 2D materials. We note that NbOX<sub>2</sub> has recently been independently identified to be a robust room temperature ferroelectric in another high-throughput study searching for 2D ferroelectric materials<sup>12</sup>. While all ferroelectric materials are piezoelectric, there is no direct correlation between the magnitude of spontaneous polarization  $|\vec{P}|$  and the magnitude of piezoelectric coefficients (see Supplementary Fig. S1). Within the NbOX<sub>2</sub> family, our calculations in fact show that the piezoelectric and ferroelectric effects have opposing trends down the halogen group. We further show that the large piezoelectric effect is independent of crystal thickness, in contrast to MoS<sub>2</sub> and similar 2D in-plane piezoelectrics, where the piezoelectricity vanishes for an even number of layers<sup>13–15</sup>. This thickness-independent piezoelectric effect is a practical advantage in isolating 2D nanoscale piezoelectrics. Experimental validations of the piezoelectric effect were carried out on few-layer NbOI<sub>2</sub> and NbOCl<sub>2</sub> crystals, where significantly larger piezoelectric coefficients were obtained compared to internal references such as In<sub>2</sub>Se<sub>3</sub> and CuInP<sub>2</sub>S<sub>6</sub> (known 2D piezoelectrics)<sup>16–20</sup>. Our findings pave the way for the development of NbOI<sub>2</sub>-based flexible nanoscale piezoelectric devices, such as high precision actuators and wearable electronics or energy-harvesters.

## Results and discussion

The workflow of our high-throughput calculations is shown in Fig. 1. Our results are publicly available in 2DMatpedia<sup>21</sup>, an open database of 2D materials that shares the same infrastructure and basic workflow as the Materials Project database<sup>22</sup>. We focus only on the 2940 “top-down” materials within the database, which are obtained by exfoliation of known bulk layered

materials, and are more likely to be dynamically stable and experimentally available. Next, we perform a rapid screening process based on the band gap and decomposition energy (both documented in 2DMatpedia<sup>21</sup>) as well as the space group (piezoelectric space groups lack inversion symmetry). A total of 225 materials pass this screening process. We then limit our high-throughput density functional perturbation theory (DFPT) calculations to materials with less than 13 atoms per unit cell (160 of the 225 materials). Following conventions for 2D materials, we compute the sheet piezoelectric stress tensor elements,  $e_{ij}$ , defined as  $\frac{\partial \vec{P}_i}{\partial \eta_j} L$ , the rate of change in polarization  $P_i$  with homogeneous strain  $\eta_j$  multiplied by the cell height  $L$ <sup>23</sup>. The index  $i$  runs from 1 to 3 ( $x, y, z$ ) and  $j$  ranges from 1 to 6 ( $xx, yy, zz, yz, xz, xy$ ) where the Voigt notation is used. A series of automated checks and analyses is carried out and the relevant data is saved into the database. 51 materials did not pass the automated checks. This is similar in proportion to those in other high throughput studies<sup>1,24,25</sup>; these materials were not studied in detail. The dynamical stability of individual materials is checked manually as needed outside this workflow.

The final results are summarized in Fig. 2a. All the 109 materials (see Supplementary Table S15 for the full list) have an  $e_{ij}$  value greater than  $0.05 \times 10^{-10} \text{ C m}^{-1}$ . These 109 2D piezoelectric materials are observed to belong to only a few space groups (Fig. 2a). Space groups 17, 26, 31, 149, 156, and 187 each have more than nine 2D piezoelectric materials. Our high throughput calculations also found that 48 of the 109 2D piezoelectric materials are not ferroelectric (see Supplementary Table S15). 2D materials previously identified to be piezoelectric<sup>23,26</sup> are also found to be piezoelectric in our calculations, with values of  $e_{ij}$  very close to their reported values (Supplementary Table S2). Most materials have maximum  $e_{ij}$  values below  $5 \times 10^{-10} \text{ C m}^{-1}$ , while a few have significantly larger  $e_{ij}$ . These larger  $e_{ij}$  values correspond to in-plane piezoelectricity.

We identify eight materials with maximum sheet  $e_{ij}$  values larger than  $10 \times 10^{-10} \text{ C m}^{-1}$ , namely, SbF<sub>3</sub>, NbOI<sub>2</sub>, NbOBr<sub>2</sub>, NbOCl<sub>2</sub>, MoBr<sub>2</sub>O<sub>2</sub>, GeSe, SbAsO<sub>3</sub>, CuInP<sub>2</sub>Se<sub>6</sub>. The structures of these eight materials (referred to as the ‘top 8’ materials) are presented in Fig. 2a–d. SbF<sub>3</sub>, which has the largest sheet  $e_{ij}$ , is found to be dynamically unstable in the monolayer form. Niobium oxydihalides, NbOX<sub>2</sub>, with X = Cl, Br, or I, have the next highest sheet  $e_{ij}$ , with NbOI<sub>2</sub> having the largest  $e_{11}$  value of  $\sim 32 \times 10^{-10} \text{ C m}^{-1}$ . We have verified explicitly that monolayer NbOI<sub>2</sub> is dynamically stable (Supplementary Fig. S2 and Fig. S3) and we expect the same to be true for the other members of the family. The exfoliation energy for NbOI<sub>2</sub> monolayers is 18.2 meV Å<sup>-2</sup>, lower than that of graphene (25.5 meV Å<sup>-2</sup>)<sup>21</sup>.

Besides the piezoelectric stress tensor elements  $e_{ij}$ , the piezoelectric strain tensor elements  $d_{ij}$  are also widely discussed in the literature. The  $d_i$  values are defined as  $\frac{\partial P_i}{\partial \sigma_j}$ , the rate of change in polarization  $P_i$  with homogeneous stress  $\sigma_j$  (see SI), and are related to  $e_{ij}$  according to  $d_{ij} = e_{ik} S_{kj}$ , where  $S_{kj}$  is the compliance tensor (the inverse of the elastic tensor). Unlike  $e_{ij}$  and  $S_{kj}$  which have a different definition for the 2D case, the  $d_{ij}$  values are defined in the same manner for both bulk and 2D (see Formalisms in SI). The  $d_{11}$  values for monolayer NbOX<sub>2</sub> are ~42, 30 and 27 pm V<sup>-1</sup> for NbOI<sub>2</sub>, NbOBr<sub>2</sub> and NbOCl<sub>2</sub>, respectively (see Supplementary Table S4). We note that all the  $d_{ij}$  values for bulk NbOX<sub>2</sub> are almost the same as for the monolayer (Table 2 and Supplementary Table S5), indicating that the piezoelectric properties of NbOX<sub>2</sub> are very similar from monolayer to bulk form. In the bulk material, the ratio of mechanical stress energy density to the electrical energy density is given by a dimensionless number  $k^2 = \frac{e_{ij} d_{ij}}{\epsilon_0 \epsilon_0}$ <sup>27,28</sup>, where  $k$  is known as the electromechanical coupling factor. We obtain an

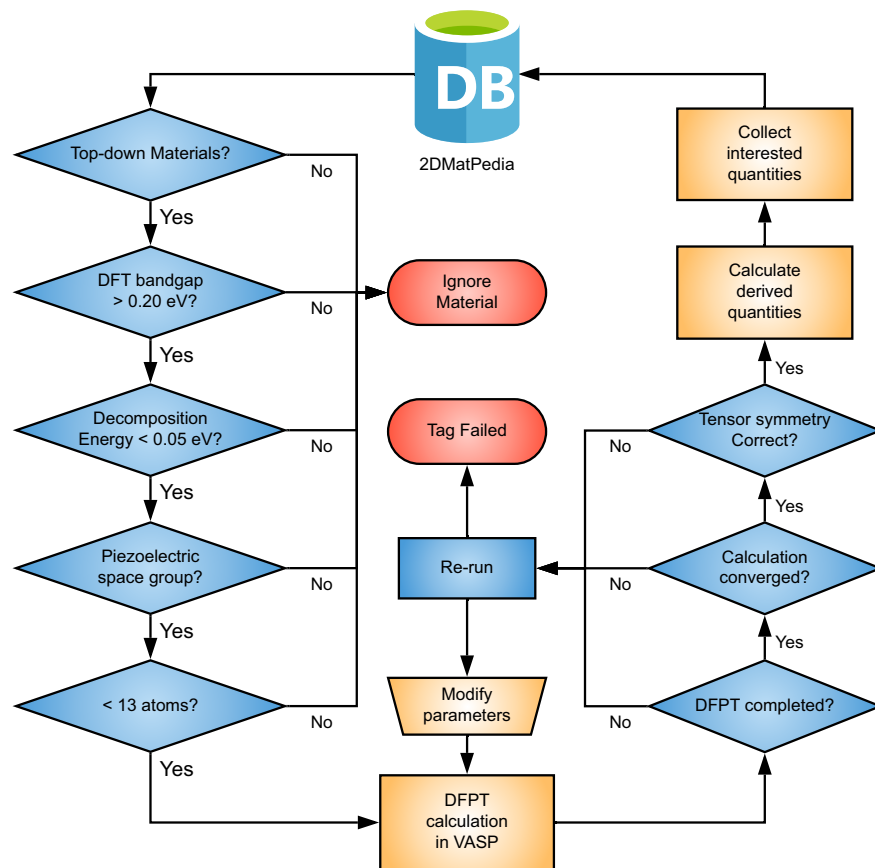


**Fig. 1 Workflow of the high-throughput calculation to screen for piezoelectric 2D materials.** We have chosen a criteria of at least 0.20 eV for the DFT band gap (large enough for operation at finite temperatures) and a decomposition energy<sup>21</sup> of < 0.05 eV to ensure thermodynamic stability.

electromechanical coupling factor of ~1.0, 0.9 and 0.9 for bulk NbOI<sub>2</sub>, NbOBr<sub>2</sub> and NbOCl<sub>2</sub>, respectively (see Supplementary Table S5). Since the maximum value of  $k$  is unity, we see that the intrinsic piezoelectricity in NbOX<sub>2</sub> provides for highly efficient interconversion between electrical and mechanical energy.

We compute the  $d_{ij}$  values for the top 8 materials (excluding SbF<sub>3</sub>) and the largest components of  $e_{ij}$  and  $d_{ij}$  are shown in Fig. 3a and Table 1. The maximum  $e_{ij}$  and  $d_{ij}$  values for other 2D piezoelectrics discussed in the literature are also plotted in Fig. 3a for comparison (see also Supplementary Table S2). Some materials such as monolayer GeSe<sup>29</sup>, As<sub>2</sub>S<sub>3</sub><sup>17</sup>, As<sub>2</sub>Se<sub>3</sub><sup>17</sup> have large  $d_{ij}$  values but small  $e_{ij}$  values, corresponding to small values of their Young's moduli. The small Young's moduli limits the amount of force exerted in electric field-induced deformations. The 2D Young's moduli  $C_{11}$  for monolayer NbOI<sub>2</sub> is ~76 N m<sup>-1</sup> (Supplementary Table S7) while the bulk value for  $C_{11}$  is ~125 GPa. A figure of merit adopted for thin-film piezoelectrics (TFFOM), when the passive elastic layer is much thicker than the piezoelectric material, is  $\frac{e_{ij}^2}{\epsilon_{ij}\epsilon_0}$ , where  $\epsilon_{ij}$  is the dielectric constant and  $\epsilon_0$  is the vacuum permittivity<sup>27,30,31</sup>. Thus, the piezoelectric stress coefficients rather than the piezoelectric strain coefficients are particularly important for 2D flexible piezoelectric applications.

It is clear that NbOX<sub>2</sub> has the largest  $e_{ij}$  values in Fig. 3a. To our knowledge, there is only one 2D material, SnSe, with a predicted  $e_{11}$  value<sup>29</sup> that is larger than NbOI<sub>2</sub>. Recent experiments on SnSe have, however, reported a much weaker piezoelectric performance<sup>9</sup> (see Supplementary Table S8), which we attribute to the Poisson effect, which reduces the effective  $e_{11}$  value of SnSe by ~51% (see Supplementary Table S1). We note that our high

throughput calculations do not account for the Poisson effect. However, the Poisson effect does not change the  $e_{11}$  values for NbOX<sub>2</sub> (see Supplementary Table S1). The figure of merit (TFFOM) for our top 8 candidates from the high throughput calculations (except SbF<sub>3</sub>) are presented in Fig. 3b and Table 1, where it is clear that NbOI<sub>2</sub> has the largest TFFOM.

In Fig. 3a, we also indicate using solid symbols the materials that are piezoelectric in the thermodynamically most stable bulk form, and hollow symbols for those that are not. NbOX<sub>2</sub> are among the minority of 2D materials that are piezoelectric both in the monolayer and in the bulk. The  $d_{ij}$  values are essentially the same for both monolayer and bulk NbOX<sub>2</sub> (see Table S9). Of the 109 piezoelectric materials that we discovered, only 30 are also piezoelectric in the bulk, according to a similar high throughput study<sup>1</sup> on the Materials Project database for bulk materials, from which the candidate monolayers were derived. A comparison of the largest  $e_{ij}$  values from the two independent studies indicates that the piezoelectric coefficients in the monolayer and the bulk are strongly correlated (see Supplementary Table S10 and Supplementary Fig. S4). The thickness-independent piezoelectric effect in NbOX<sub>2</sub> implies that few-layer NbOX<sub>2</sub> can be prepared for nanoscale piezoelectric applications without the need for a pre-selection process based on the number of layers.

The atomic structure of monolayer NbOX<sub>2</sub> is shown in Fig. 2b, c. Along the  $y$ -direction, Peierls distortion results in alternating Nb-Nb distances, and along the  $x$ -direction, the Nb atom is displaced away from the high symmetry position where  $\delta x = x_1 - x_2$  (Fig. 2d), giving rise to a spontaneous polarization (Table 2). The degree of structural asymmetry along the  $x$ -direction is largest for NbOCl<sub>2</sub> and smallest for NbOI<sub>2</sub> (Fig. 2d). The asymmetry along the  $x$ -direction can be

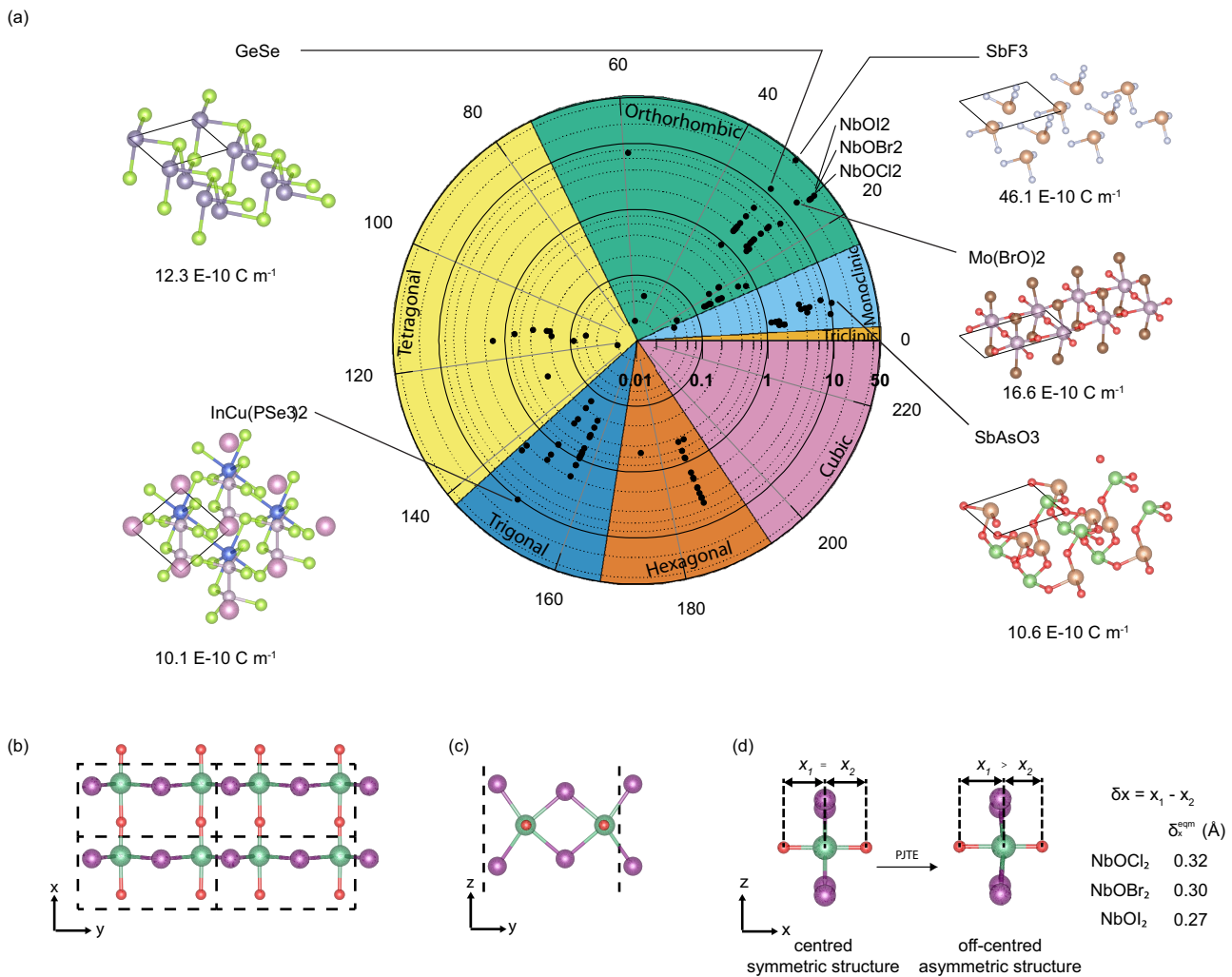


**Fig. 2 Maximum sheet piezoelectric tensor elements and atomic structures of selected materials.** **a** High-throughput calculation results for maximum sheet piezoelectric stress tensor elements ( $e_{ij}$ ). The radial axis represents the magnitude of  $e_{ij}$  in units of  $10^{-10} \text{ C m}^{-1}$  on a log scale and the angular axis represents the 230 space groups. Materials with  $e_{ij}$  larger than  $10 \times 10^{-10} \text{ C m}^{-1}$  are labeled and their atomic structures are presented. The maximum  $e_{ij}$  corresponds to  $e_{26}$  for SbF<sub>3</sub> and to  $e_{11}$  for NbOX<sub>2</sub>. Atomic structures of selected materials are also presented. **b** Top view and **c** Side view down the x-axis to the atomic structure of monolayer NbOX<sub>2</sub> (X = I, Br, Cl). Dark green balls denote Nb atoms; purple balls denote halogens; red balls denote O atoms. Dashed lines mark the unit cell boundaries. **d** Schematic, viewed along y-axis, showing relative displacement of Nb atoms along the x-axis away from the high symmetry position where  $\delta x = 0 \text{ \AA}$ , to the equilibrium position where  $\delta x = \delta_x^{\text{eqm}}$ . Additional structural parameters are provided in Supplementary Table S3. PJTE refers to the pseudo-Jahn-Teller effect.

explained by the pseudo-Jahn-Teller effect (PJTE)<sup>32</sup>, where mixing between the valence O  $p$  orbitals and conduction Nb  $d$  orbitals results in a more energetically favorable configuration accompanied by structural distortion as well as increased Nb-O bond strengths and covalency (see SI for details). The piezoelectric tensor elements in Table 2 reflect the strong in-plane anisotropy of the system. In bulk NbOX<sub>2</sub>, the directions for the inversion-symmetry-breaking distortions are the same in all layers, and the difference in  $\delta_x^{\text{eqm}}$  is within 0.002 Å in the bulk and monolayer systems (Supplementary Table S3 and Table S11). Thus, the piezoelectric properties are similar in bulk, monolayer and thin film form.

Quantitative measurements of piezoelectric coefficients in 2D materials are challenging, since any small parasitic vibration, boundary effect, or electrostatic force during the piezoelectric measurement (especially the single-point measurement) significantly affects the accuracy of the measured values<sup>10</sup>. To provide quantitative information about the piezoelectric coefficients within the family of NbOX<sub>2</sub>, and to compare the piezoelectric coefficients with those of other known 2D piezoelectrics,  $\alpha$ -In<sub>2</sub>Se<sub>3</sub>

and CuInP<sub>2</sub>S<sub>6</sub>, we performed laser scanning vibrometer (LSV)<sup>33</sup> measurements on thick bulk-like samples. All these materials are also piezoelectric in the bulk. The existence of ferroelectricity and piezoelectricity in thin films of NbOX<sub>2</sub> was demonstrated using piezoresponse force microscopy (PFM) for thicknesses down to sub-10 nm.

We synthesize large-sized NbO<sub>2</sub> and NbOCl<sub>2</sub> crystals grown by the chemical vapor transport method (refer to Methods for details). The crystal structures of the as-grown NbO<sub>2</sub> and NbOCl<sub>2</sub> crystals are confirmed by single-crystal X-ray diffraction (SC-XRD) (Supplementary CIFs and Supplementary Table S11). The crystallographic directions of the NbOX<sub>2</sub> crystals are also identified from the SC-XRD analysis. These room-temperature SC-XRD studies show that the crystal belongs to polar space group C2 (No. 5), hence providing further evidence that the ground state of bulk NbOX<sub>2</sub> is ferroelectric (refer to Supplementary Note 1: Polarization switching in NbOX<sub>2</sub> and Supplementary Note 2: Ferroelectric-paraelectric phase transition in NbO<sub>2</sub> for ferroelectric data).

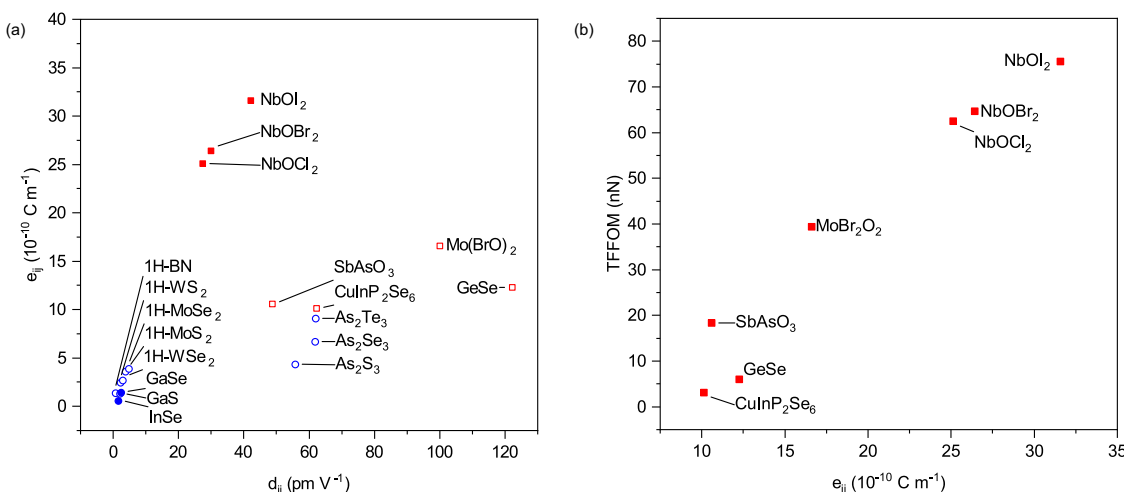


**Fig. 3 Thin film figure of merit (TFFOM) and spontaneous polarizations.** **a** Plot of maximum sheet piezoelectric stress tensor elements ( $e_{ij}$ ) and corresponding piezoelectric strain tensor elements ( $d_{ij}$ ) for various 2D materials. For additional notes on GeSe, please see Supplementary Table S1. **b** Plot of TFFOM and maximum  $e_{ij}$  of materials highlighted in Fig. 2a. In **a**, solid symbols denote materials that are piezoelectric in the thermodynamically most stable bulk form, as documented in the Materials Project database<sup>1</sup>; hollow symbols denote those that are not. Blue dots denote data points obtained from other studies<sup>17,23,26,29,49</sup> listed in Supplementary Table S2. Our computed  $e_{ij}$  values for these materials are also provided in Supplementary Table S2 for comparison.

**Table 1 Materials with  $e_{ij} > 10 \times 10^{-10} \text{ C m}^{-1}$ .**

Material	ij	$e_{ij} (10^{-10} \text{ C m}^{-1})$	$d_{ij} (\text{pm V}^{-1})$	$C_{ij} (\text{N m}^{-1})$	TFFOM (nN)
NbOI <sub>2</sub>	11	31.6	42.2	75.6	71.7
NbOBr <sub>2</sub>	11	26.4	30.0	89.0	63.2
NbOCl <sub>2</sub>	11	25.1	27.4	92.9	59.6
MoBr <sub>2</sub> O <sub>2</sub>	22	16.6	100.1	33.8	39.3
GeSe	22	12.3	122.2	18.2	6.0
SbAsO <sub>3</sub>	11	10.6	48.7	22.3	18.4
CuInP <sub>2</sub> Se <sub>6</sub>	22	10.1	62.3	44.5	3.1

$e_{ij}$  is the piezoelectric stress tensor element,  $d_{ij}$  is the piezoelectric strain tensor element,  $C_{ij}$  is the elastic tensor element, and TFFOM is the figure of merit for thin film piezoelectric devices.<sup>27</sup> Our computed in-plane dielectric constant of NbOX<sub>2</sub> is 12–15 (see Supplementary Table S6).

**Table 2 Piezoelectric tensor elements and spontaneous polarizations of NbOX<sub>2</sub>.**

Formula	$e_{11}$	$e_{12}$	$e_{13}$	$e_{26}$	$e_{35}$	$d_{11}$	$d_{12}$	$d_{26}$	$P_x$
NbOCl <sub>2</sub>	25.1	-1.1	-0.4	0.8	0.0	27.4	-4.1	5.4	185
NbOBr <sub>2</sub>	26.4	-1.0	-0.4	0.8	0.0	30.0	-4.1	5.8	170
NbOI <sub>2</sub>	31.6	-1.0	-0.3	0.7	0.0	42.2	-5.1	5.2	143

Sheet piezoelectric stress tensor elements  $e_{ij}$  are in units of  $10^{-10} \text{ C m}^{-1}$  and piezoelectric strain tensor elements  $d_{ij}$  are in pm V<sup>-1</sup>. Piezoelectric tensor elements that are zero due to symmetry of the space group are omitted here. Spontaneous polarization along the x-direction ( $P_x$ ) in pC m<sup>-1</sup> is calculated as the difference between the polarization of the equilibrium and symmetric structures.

To investigate if ultrathin NbOX<sub>2</sub> is ferroelectric, nanosheets were exfoliated from bulk crystals via the Scotch tape method and then transferred onto gold (Au) substrates (Supplementary Fig. S5) for PFM characterization. NbOX<sub>2</sub> is thermodynamically stable and all experimental measurements were performed under ambient conditions. In PFM, an AC voltage is applied between a conductive sharp tip and the bottom electrode of a piezoelectric sample to induce local mechanical deformations by means of the converse piezoelectric effect<sup>34,35</sup>. Scanning tip-induced hysteretic switching events were recorded using spectroscopic PFM (Supplementary Note 1: Polarization switching in NbOX<sub>2</sub>, and Fig. S19). The ferroelectric-paraelectric phase transition in NbOI<sub>2</sub> was further observed using temperature-dependent differential

scanning calorimetry and second harmonic generation measurements (Supplementary Note 2: Ferroelectric-paraelectric phase transition in NbOI<sub>2</sub>, and Fig. S20).

Figure 4a presents an 82-nm-thick NbOI<sub>2</sub> flake with corresponding phase (Fig. 4b) and amplitude (Fig. 4c) images constructed using an in-plane (IP) PFM output channel. A clear contrast exists between different domains in the lateral phase and amplitude. The PFM phase indicates the direction of the ferroelectric polarization, whereas the PFM amplitude reflects the magnitude of the local piezoelectric response. The bright and dark contrasts in the PFM phase image indicate that there exist two oppositely polarized ferroelectric domains, characterized by a ~180° phase difference (Fig. 4d). Supplementary Fig. S6–S10 display additional PFM data for NbOI<sub>2</sub> and NbOCl<sub>2</sub>, demonstrating piezoelectric response down to 4.3 nm-thickness for NbOI<sub>2</sub>.

To confirm the in-plane piezoelectric anisotropy, vector PFM<sup>36,37</sup> is conducted on 10-nm-thick NbOI<sub>2</sub> (Fig. 4e–h) and 17-nm-thick NbOCl<sub>2</sub> (Supplementary Fig. S11) flakes with height profiles shown in Supplementary Fig. S12. As expected, the in-plane PFM response is strongest when the polar axis is orthogonal to the cantilever long axis, as shown in Fig. 4e ( $\varphi$  is the polarization angle relative to the cantilever long axis). When the sample is rotated by 90 degrees, no lateral PFM contrast is observed (Fig. 4g, h). In addition, the out-of-plane piezoresponse for the NbOX<sub>2</sub> nanoflakes are typically negligible, as displayed in Supplementary Fig. S6 and Figs. S8–S10. The vector PFM results as well as predominantly in-plane response confirms that the physical origin of the PFM signals is piezoelectricity rather than electrostatic tip-sample interactions<sup>38,39</sup>.

We quantified the lateral ( $d_{11}$ ,  $d_{22}$ ) and vertical ( $d_{33}$ ) piezoelectric coefficients of NbOX<sub>2</sub> through laser scanning vibrometer (LSV)<sup>33</sup> measurements. LSV is a non-contact optical technique that measures the vibration velocity of a moving piezoelectric surface by monitoring the interference pattern (Doppler frequency shift) between the scattered light and the incident light. By integrating the vibration velocity, the mechanical displacement in response to an applied electric field can be determined. The LSV vibration modalities are measured along the x ( $d_{11}$ ) (Fig. 5a, d), y ( $d_{22}$ ) (Fig. 5b, e) and z ( $d_{33}$ ) (Fig. 5c, f) directions of NbOX<sub>2</sub>. Consistent with the

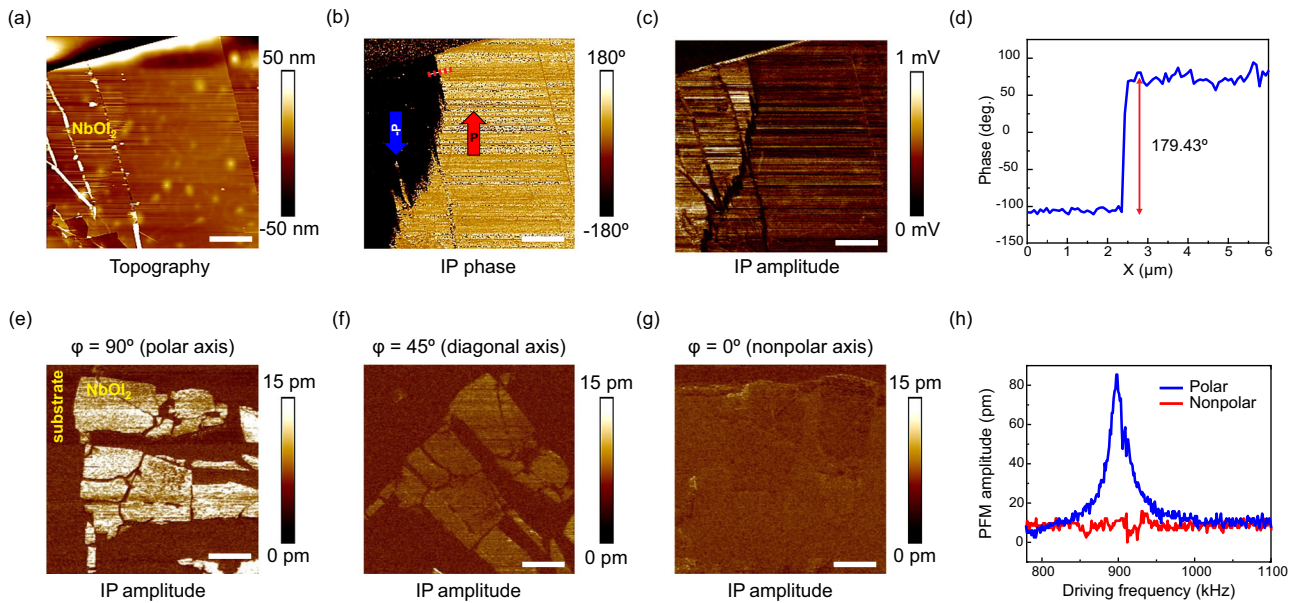


**Fig. 4 Piezoelectric force microscopy (PFM) investigation of thin NbOX<sub>2</sub>.** **a** Topography, **b** In-plane (IP) phase, **c** IP amplitude, and **d** phase profile across antiparallel polarization states of 82-nm-thick NbO<sub>2</sub> flake. **e–g** Vector PFM IP amplitude images of 10-nm-thick NbO<sub>2</sub> showing spontaneous polarization at 90° **e**, 45° **f**, and 0° **g** angles relative to the cantilever long axis. **h** PFM amplitude profiles along the polar and nonpolar axes of the 10-nm-thick NbO<sub>2</sub> flake. Scale bars: 4 μm. Drive voltage: **b, c** 5 V, **e–h** 3 V. Drive frequency: **b, c** 65 kHz, **e** 827 kHz, **f** 974 kHz, **g** 890 kHz.

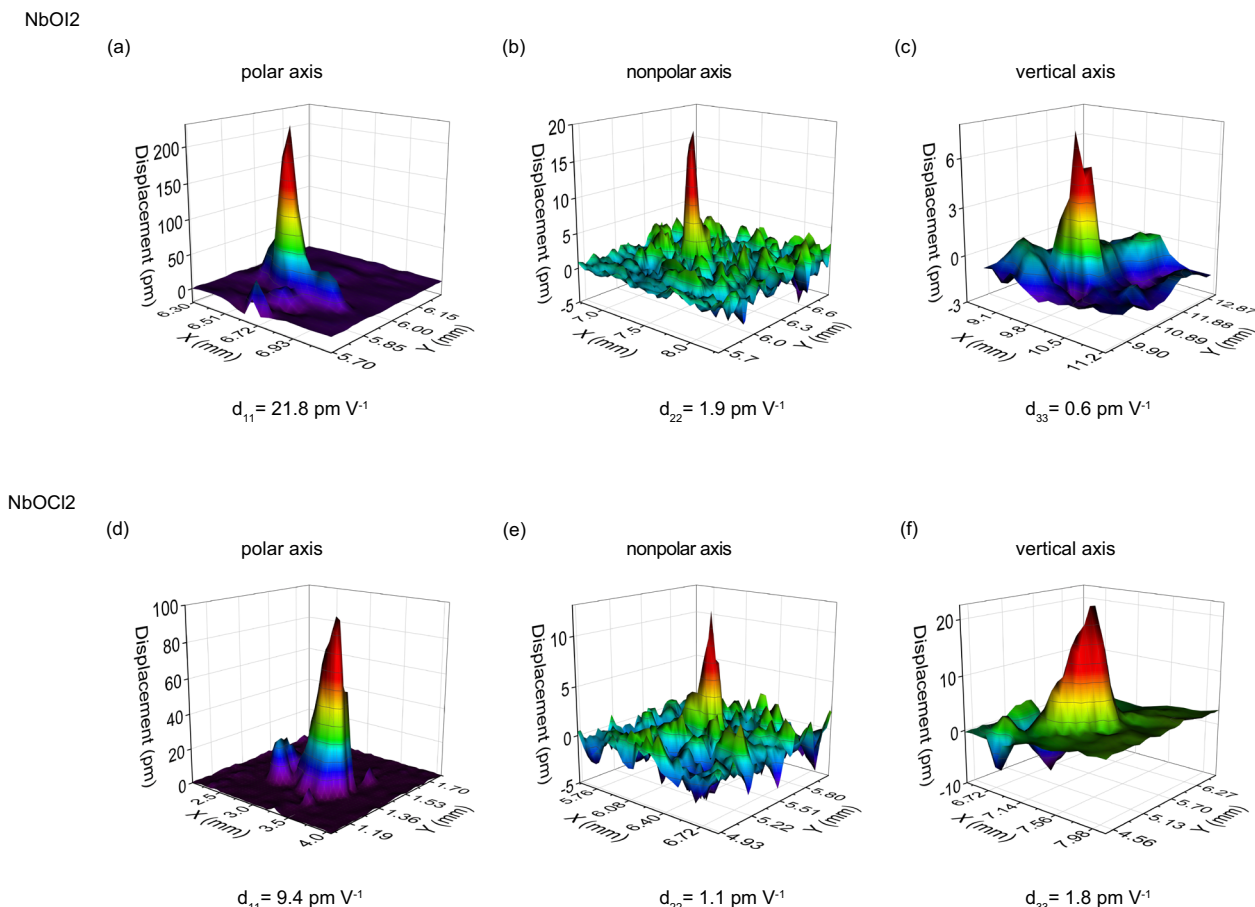


**Fig. 5 Evaluation of the piezoelectric coefficients of NbOX<sub>2</sub> using a laser scanning vibrometer (LSV).** 3D graphs of the instantaneous vibration when the displacement magnitude reaches the maximum under the sine-wave driving electrical signal. **a, d** Measurement along the lateral polar direction ( $d_{11}$ ). **b, e** Measurements along the lateral nonpolar direction ( $d_{22}$ ). **c, f** Measurements along the vertical nonpolar direction ( $d_{33}$ ).

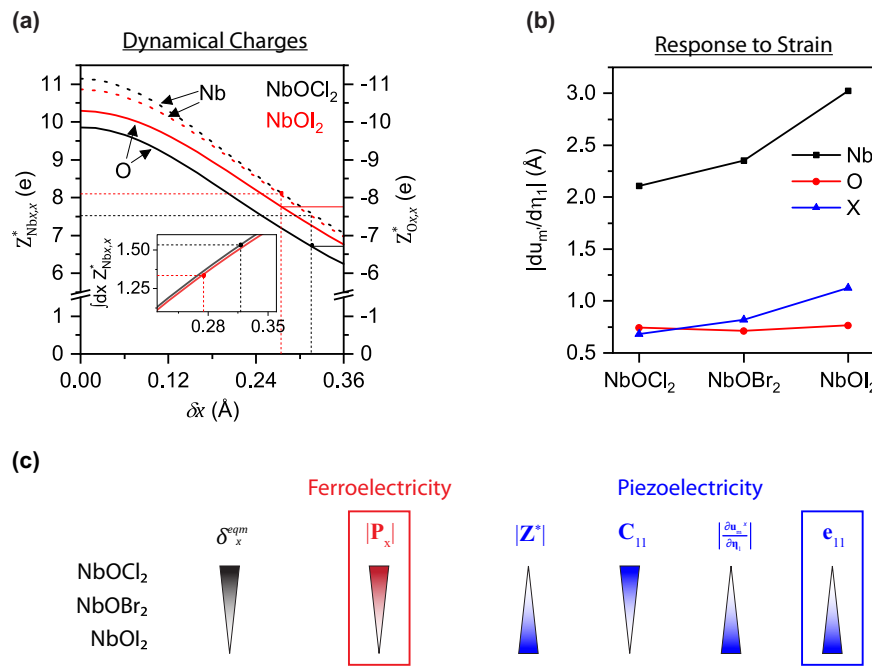


**Fig. 6 Understanding the origin of piezoelectric and ferroelectric effects in the  $\text{NbOX}_2$  family.** **a** Dynamical charges for Nb and O,  $Z^*_{Nb,x}$  and  $Z^*_{O,x}$ , as a function of  $\delta x$ , the difference between the longer and shorter Nb-O bonds. The inset shows the integral of  $Z^*_{Nb,x}$  with respect to the  $x$ -displacement away from the high-symmetry site. In both the main figure and the inset, dashed lines indicate the values in the equilibrium structures. **b**  $|du_m/d\eta_i|$  in the equilibrium structures of  $\text{NbOX}_2$ , indicating the rate of change of  $x$ -displacement of each atom (Nb, O, or X) with strain in the  $x$ -direction.  $\text{NbOI}_2$  has the largest lattice response to strain, due to the smaller stiffness tensor elements and weaker Nb-O bonds. **c** Schematic illustrating the origins of the trends in ferroelectricity and piezoelectricity in  $\text{NbOX}_2$ .

vector PFM data, the LSV vibration modalities further confirm the anisotropy of the piezoelectric response in  $\text{NbOX}_2$ . Our measurements reveal that  $\text{NbOI}_2$  exhibits stronger piezoelectric effects than  $\text{NbOCl}_2$  (the  $d_{11(\text{eff})}$  values are  $\sim 21.8 \text{ pm V}^{-1}$  for  $\text{NbOI}_2$  and  $\sim 9.4 \text{ pm V}^{-1}$  for  $\text{NbOCl}_2$ ), consistent with our theoretical predictions (Table 2). These values are likely to be underestimated due to the significant electric leakage of the  $\text{NbOX}_2$  samples. Despite this, our measured  $d_{11(\text{eff})}$  piezoelectric coefficients are larger than the largest  $d_{ij(\text{eff})}$  values we measured for common 2D ferroelectrics, such as  $\alpha\text{-In}_2\text{Se}_3$  and  $\text{CuInP}_2\text{S}_6$  (Supplementary Fig. S13). There is also a strong correlation between the measured  $d_{ij(\text{eff})}$  values and the corresponding computed values (Supplementary Fig. S14). These LSV results show that  $\text{NbOX}_2$  has superior piezoelectric performance compared to other 2D material piezoelectrics.

We analyze the origins of the large piezoelectric and ferroelectric effects in  $\text{NbOX}_2$ , and their trends down the halogen group. The large values of  $e_{11}$  arise predominantly from the lattice response to the applied strain (see Supplementary Table S12). This dominant ionic contribution can be written in an implied sum notation as

$$e_{ij}^{ion} = Z_{m,i}^* \frac{\partial \mathbf{u}_m}{\partial \boldsymbol{\eta}_j} \quad (1)$$

where  $Z_{m,i}^*$  is the dynamical charge ( $m$  is a composite label for atom and displacement direction and  $i$  is the direction of the polarization),  $\mathbf{u}$  is the position vector of the atom and  $\boldsymbol{\eta}_j$  denotes the applied strain. The dynamical charge is defined as the rate of change of polarization with atomic displacement, while  $\frac{\partial \mathbf{u}_m}{\partial \boldsymbol{\eta}_j}$  quantifies the rate of change in atomic displacement with applied strain. The dynamical charges play an important role in both the piezoelectric and ferroelectric effects.

Figure 6a shows that the dynamical charges in the  $x$ -direction for Nb and O in  $\text{NbOCl}_2$  and  $\text{NbOI}_2$ , decrease in magnitude

as the off-center displacement,  $\delta x$ , increases. These dynamical charges are significantly larger in magnitude than their expected formal oxidation states (+4 for Nb and -2 for O) as well as their estimated static charges (see Supplementary Fig. S15). The anomalous dynamical charges can be attributed to the partial covalency present in the Nb-O bonds, which is more significant in  $\text{NbOI}_2$  due to the smaller electronegativity of I compared to Cl (see SI and Supplementary Fig. S16)<sup>40</sup>. The smaller off-center distortion in  $\text{NbOI}_2$  (smallest  $\delta_x^{eqm}$ ) further increases the dynamical charges at equilibrium compared to those for  $\text{NbOCl}_2$ , contributing to the superior piezoelectric performance of  $\text{NbOI}_2$ . On the other hand, the integral of the dynamical charges with respect to atomic displacements, from the centered symmetric structure to the equilibrium off-centered structure, gives the magnitude of the spontaneous polarization at equilibrium, and the larger  $\delta_x^{eqm}$  for  $\text{NbOCl}_2$  results in a larger  $|\vec{P}|$  compared to  $\text{NbOI}_2$  (Fig. 6a inset).

The larger magnitudes of  $\frac{\partial \mathbf{u}_m}{\partial \boldsymbol{\eta}_1}$  (the superscript for  $m$  representing displacements in the  $x$ -direction) for Nb and X atoms in  $\text{NbOI}_2$  (Fig. 6b) further contribute to the large  $e_{11}$  value for  $\text{NbOI}_2$  (see also Supplementary Table S13). The observed trend in  $\frac{\partial \mathbf{u}_m}{\partial \boldsymbol{\eta}_1}$  for Nb and X can be traced to the degree of bond covalency/ionicity in these systems, the more ionic  $\text{NbOCl}_2$  having stiffer bonds and hence smaller magnitudes of  $\frac{\partial \mathbf{u}_m}{\partial \boldsymbol{\eta}_1}$ . This trend can also be observed in the decrease in Young's modulus  $C_{11}$  down the halogen group (see Supplementary Table S7). Figure 6c summarizes the different factors that contribute to  $e_{11}$  being largest for  $\text{NbOI}_2$ , in contrast to  $|\vec{P}|$  being largest for  $\text{NbOCl}_2$ .

While our top candidates for monolayer piezoelectrics all exhibit in-plane piezoelectricity, we comment that out-of-plane piezoelectricity (non-zero  $e_{3j}$ ) in the 2D monolayers is found in 46 of the materials in our database, as shown in Supplementary Fig. S17. Most of the non-zero  $e_{3j}$  values have magnitudes less

than  $1 \times 10^{-10} \text{ C m}^{-1}$ , with a few exceptions having values up to  $\sim 4 \times 10^{-10} \text{ C m}^{-1}$ , as indicated in Supplementary Fig. S17 and Supplementary Table S14. It has been reported that bulk layered CuInP<sub>2</sub>S<sub>6</sub> has an electromechanical coupling factor of 0.7–0.9, corresponding to a large out-of-plane piezoelectric coefficient which originates from the deformation of the van der Waals gap<sup>41</sup>. Such a mechanism has not been considered in our study on monolayers. Our findings that monolayer and bulk NbOI<sub>2</sub> have exceptionally large in-plane piezoelectric effects are especially important for actuator applications that require pure in-plane movement<sup>42</sup>.

In summary, we have identified, from among 2940 candidate monolayers, NbOI<sub>2</sub> as the material with the largest piezoelectric stress coefficient. Furthermore, NbOI<sub>2</sub> is one of the minority of monolayer piezoelectrics that is also piezoelectric in the bulk. Our experimentally measured values of piezoelectric strain coefficients are within a factor of two of the predicted value for NbOI<sub>2</sub>, and are much larger than those measured concurrently for  $\alpha$ -In<sub>2</sub>Se<sub>3</sub> and CuInP<sub>2</sub>S<sub>6</sub>. We have also verified in-plane ferroelectricity in NbOI<sub>2</sub>. While NbOI<sub>2</sub> has the largest piezoelectric coefficients, NbOCl<sub>2</sub> has the largest spontaneous polarization. The excellent piezoelectric and ferroelectric effects in NbOX<sub>2</sub>, as well as their trends down the halogen group, are rationalized on the basis of bond covalency and symmetry-breaking structural distortions in these materials. The structure-property correlations obtained here provide guidance for the design of functional piezoelectric and ferroelectric materials, while the discovery of 2D NbOI<sub>2</sub> as a high-performance piezoelectric paves the way for 2D piezoelectric devices.

## Methods

**Computational methods.** For the high-throughput DFPT calculations, only materials from space groups 1, 3–9, 16–46, 75–82, 89–122, 143–146, 149–161, 168–174, 177–190, 195–199, 207–220<sup>1</sup> are selected. These space groups lack inversion symmetry. DFPT calculations are performed with the plane-wave pseudopotential code VASP<sup>43,44</sup>, employing the generalized gradient approximation (GGA) for the exchange-correlation functional<sup>45</sup>. We use an energy cutoff of 520 eV, a Monkhorst-Pack k-point mesh with a density of 1500 per reciprocal atom (number of atoms per cell multiplied by the number of k-points)<sup>1</sup>, a force convergence criterion of 0.005 eV Å<sup>-1</sup> and a criterion of 10<sup>-10</sup> eV for the convergence of the self-consistent cycle. The calculations are performed with a vacuum separation of about 20 Å between the 2D materials.

We modify the standard workflows<sup>46,47</sup> developed by Materials Project<sup>1,22</sup> to include additional post processing steps that convert the 3D piezoelectric tensor elements to 2D sheet piezoelectric tensor elements in the unit of C m<sup>-1</sup> by multiplying the former with the cell height. Other results, including the dynamical charge tensor (also known as the Born effective charge tensor), dielectric tensor (ionic and electronic contributions), Γ point phonon eigenvalue and eigenvectors, full piezoelectric tensor (in both C m<sup>-2</sup> and C m<sup>-1</sup>), maximum (sheet) piezoelectric tensor elements in C m<sup>-2</sup> (C m<sup>-1</sup>) and maximum (sheet) out-of-plane piezoelectric tensor elements in C m<sup>-2</sup> (C m<sup>-1</sup>) are also captured. Our workflow also inherits the consistency checks and filters in the Materials Project Workflow<sup>1</sup> to detect errors arising from DFT calculation and convergence-related issues.

For the targeted study on NbOX<sub>2</sub>, Monkhorst-Pack k point meshes of 12 × 6 × 1 including the Γ point are used. The atomic coordinates are fully relaxed using the conjugate gradient scheme until the maximum energy difference between iterations is less than 10<sup>-8</sup> eV and the residual force is less than 0.001 eV Å<sup>-1</sup>. Other parameters are inherited from the high-throughput calculations.

For calculations with fixed  $\delta x$ , the x-coordinates of the atomic positions are fixed while the y and z coordinates are allowed to relax. The lattice constants are kept fixed.  $\frac{\partial u_{ij}}{\partial x_i}$  is obtained by applying strain in the x-direction and allowing the atoms to relax.

The elastic properties of NbOX<sub>2</sub> are obtained using a finite difference method as implemented in VASP. The elastic tensors are adapted for 2D materials according to the treatment by Choudhary et al.<sup>48</sup>.

The piezoelectric strain tensor ( $d_{ij}$ ) is calculated from piezoelectric stress tensor ( $e_{ij}$ ) through Supplementary Equation S7. Elements in  $S_{ij}$  related to the z-direction are set to 0.

**Synthesis of single crystals of NbOI<sub>2</sub> and NbOCl<sub>2</sub>.** Crystalline NbOI<sub>2</sub> and NbOCl<sub>2</sub> are grown by the chemical vapor transport method. High-purity Nb (film), iodine (crystals), and Nb<sub>2</sub>O<sub>5</sub> (powder) with a stoichiometric ratio Nb:O:I = 1:1:2 are used as precursors for the growth of NbOI<sub>2</sub>. The mixture of precursors is placed in a quartz ampule, and the ampule is sealed after being evacuated (10<sup>-5</sup> Torr).

Similarly, Nb, NbCl<sub>5</sub> (powder), and Nb<sub>2</sub>O<sub>5</sub> are used to grow NbOCl<sub>2</sub>. The sealed quartz ampules are placed at the center of a horizontal dual-zone furnace. Both heating zones were slowly heated to 600 °C and holding for 5 days. The ampules are then slowly cooled for 10 days with slightly different rates at the hot (1.2 °C h<sup>-1</sup>) and cold (1.5 °C h<sup>-1</sup>) zones. After the slow-cooling process, the furnace is turned off allowing the ampules to cool down naturally. Crystals are extracted from the opened ampules under inert conditions of an N<sub>2</sub>-filled glove box and then stored for future use.

**X-ray diffraction (XRD) measurements.** Single crystal X-ray diffractions of bulk NbOCl<sub>2</sub> and NbOI<sub>2</sub> crystals are measured using a four circles goniometer Kappa geometry, Bruker AXS D8 Venture, equipped with a Photon 100 CMOS active pixel sensor detector. A molybdenum monochromatized ( $\lambda = 0.71073 \text{ \AA}$ ) X-Ray radiation is used for the measurement. The frames are integrated with the Bruker SAINT software using a narrow-frame algorithm. Data are corrected for absorption effects using the Multi-Scan method (SADABS). The structures are solved in the monoclinic unit cell and refined using the SHELXT, VERSION 2014/5 Software. The final anisotropic refinement of the structures is performed by least squares procedures on weighted F<sup>2</sup> values using the SHELXL-2014/7 (Sheldrick, 2014) included in the APEX3 v2016, 9.0, AXS Bruker program.

**Piezoresponse force microscopy (PFM) characterization.** Mechanical exfoliation is performed by peeling off as-grown crystals using the Scotch tape method. Exfoliated crystals are directly transferred onto fresh gold (Au) substrates for PFM characterization. PFM images are obtained using a Bruker Dimension Icon AFM in contact mode. Pt/Ir-coated silicon tips with a radius of 20 nm and a force constant of 0.4 N m<sup>-1</sup> are used for the PFM measurements. The drive frequency and drive amplitude for the PFM images are ~30–975 kHz and 2.5–10 V, respectively. The PFM amplitude is expressed in pm or mV units depending on the selected PFM output channel. Angular-resolved vector PFM was performed by rotating the NbOX<sub>2</sub> samples with respect to the cantilever axis. The spectroscopic PFM hysteresis loops were acquired with ±10 V DC sweeps while applying an AC voltage of 5 V. PFM was operated in various contact scanning modes to measure both in-plane (buckling and twisting/torsional modes) and out-of-plane (deflection mode) components of the piezoresponse independently and simultaneously.

**Laser scanning vibrometer (LSV) measurements.** The effective piezoelectric coefficients of NbOX<sub>2</sub>,  $\alpha$ -In<sub>2</sub>Se<sub>3</sub>, and CuInP<sub>2</sub>S<sub>6</sub> (CIPS) are measured with a laser scanning vibrometer (OFV-3001-SF6, PolyTech GmbH) after the crystals are DC poled under 150 V along the relevant crystallographic direction for 5 min. The LSV data are collected along the x ( $d_{11}$ ), y ( $d_{22}$ ) and z ( $d_{33}$ ) directions of NbOX<sub>2</sub> and along the z ( $d_{33}$ ) directions of  $\alpha$ -In<sub>2</sub>Se<sub>3</sub> and CIPS under a unipolar AC signal of amplitude 10 V at 8 kHz through silver electrodes. The  $\alpha$ -In<sub>2</sub>Se<sub>3</sub> and CuInP<sub>2</sub>S<sub>6</sub> crystals were purchased from HQGraphene. The effective piezoelectric coefficients are deduced from the profile analysis of the instantaneous displacement data to determine the strain generated under the sine-wave driving electrical signal.

**Ferroelectric Measurements.** Polarization–electric field (P–E) loops were recorded using a ferroelectric tester (Precision Multiferroic II, Radian Technologies). Lateral NbOI<sub>2</sub> devices are fabricated by transferring NbOI<sub>2</sub> flakes onto interdigitated platinum (Pt) electrodes (10/5 μm, electrode/gap) via poly (dimethyl siloxane) (PDMS) stamp-transfer method. The Pt contacts (70 nm thick) are patterned on thermally grown silicon dioxide using electron beam lithography, electron beam evaporation, and lift-off process. A transfer station with an optical microscope and a rotating stage is used to transfer the NbOI<sub>2</sub> flakes in such a way that the device's lateral electrical field is aligned along either the in-plane polar or nonpolar axis of the transferred flakes. The P–E loop is acquired with ±10 V sweeps.

Differential scanning calorimetry (DSC) analysis was performed under a nitrogen atmosphere with a heating rate of 10 °C min<sup>-1</sup> using Mettler-Toledo DSC.

**Reporting summary.** Further information on research design is available in the Nature Research Reporting Summary linked to this article.

## Data availability

The datasets generated during and/or analyzed during the current study are available from the corresponding author on reasonable request.

## Code availability

The code used in this work is modified from the open-source tools developed by Materials Project, in particular, Python Materials Genomics (<http://pymatgen.org/>) and Atomate (<https://atomate.org/>). The versions used in this work are pymatgen/2018.8.10 and atomate/0.8.2 for all the calculations.

Received: 9 January 2022; Accepted: 15 March 2022;

Published online: 07 April 2022

## References

1. de Jong, M., Chen, W., Geerlings, H., Asta, M. & Persson, K. A. A database to enable discovery and design of piezoelectric materials. *Sci. Data* **2**, 150053 (2015).
2. Gullapalli, H. et al. Flexible piezoelectric ZnO–paper nanocomposite strain sensor. *Small* **6**, 1641–1646 (2010).
3. Wang, X. et al. Piezoelectric field effect transistor and nanoforce sensor based on a single ZnO nanowire. *Nano Lett.* **6**, 2768–2772 (2006).
4. Doll, J. C., Peng, A. W., Ricci, A. J. & Pruitt, B. L. Faster than the speed of hearing: nanomechanical force probes enable the electromechanical observation of cochlear hair cells. *Nano Lett.* **12**, 6107–6111 (2012).
5. Yun, Y. et al. A multi-wall carbon nanotube tower electrochemical actuator. *Nano Lett.* **6**, 689–693 (2006).
6. Romano, G. et al. Piezoelectric potential in vertically aligned nanowires for high output nanogenerators. *Nanotechnology* **22**, 465401 (2011).
7. Wang, Z. L. & Song, J. Piezoelectric nanogenerators based on zinc oxide nanowire arrays. *Science* **312**, 242–246 (2006).
8. Wang, X. et al. Subatomic deformation driven by vertical piezoelectricity from CdS ultrathin films. *Sci. Adv.* **2**, e1600209 (2016).
9. Li, P. et al. A self-powered 2D-material sensor unit driven by a SnSe piezoelectric nanogenerator. *J. Mater. Chem. A* **9**, 4716–4723 (2021).
10. Chen, Q. N., Ou, Y., Ma, F. & Li, J. Mechanisms of electromechanical coupling in strain based scanning probe microscopy. *Appl. Phys. Lett.* **104**, 242907 (2014).
11. Hinchet, R., Khan, U., Falconi, C. & Kim, S.-W. Piezoelectric properties in two-dimensional materials: Simulations and experiments. *Mater. Today* **21**, 611–630 (2018).
12. Jia, Y., Zhao, M., Gou, G., Zeng, X. C. & Li, J. Niobium oxide dihalides NbOX<sub>2</sub>: a new family of two-dimensional van der Waals layered materials with intrinsic ferroelectricity and antiferroelectricity. *Nanoscale Horiz.* **4**, 1113–1123 (2019).
13. Zhu, H. et al. Observation of piezoelectricity in free-standing monolayer MoS<sub>2</sub>. *Nat. Nanotechnol.* **10**, 151–155 (2015).
14. Esfahani, E. N., Li, T., Huang, B., Xu, X. D. & Li, J. Y. Piezoelectricity of atomically thin WSe<sub>2</sub> via laterally excited scanning probe microscopy. *Nano Energy* **52**, 117–122 (2018).
15. Ares, P. et al. Piezoelectricity in monolayer hexagonal boron nitride. *Adv. Mater.* **32**, 1905504 (2020).
16. Zhou, Y. et al. Out-of-plane piezoelectricity and ferroelectricity in layered alpha-In<sub>2</sub>Se<sub>3</sub> nanoflakes. *Nano Lett.* **17**, 5508–5513 (2017).
17. Gao, W. & Chelikowsky, J. R. Prediction of intrinsic ferroelectricity and large piezoelectricity in monolayer arsenic chalcogenides. *Nano Lett.* **20**, 8346–8352 (2020).
18. Ding, W. et al. Prediction of intrinsic two-dimensional ferroelectrics in In<sub>2</sub>Se<sub>3</sub> and other III<sub>2</sub>-VI<sub>3</sub> van der Waals materials. *Nat. Commun.* **8**, 14956 (2017).
19. Liu, F. et al. Room-temperature ferroelectricity in CuInP<sub>2</sub>S<sub>6</sub> ultrathin flakes. *Nat. Commun.* **7**, 12357 (2016).
20. Cui, C., Xue, F., Hu, W.-J. & Li, L.-J. Two-dimensional materials with piezoelectric and ferroelectric functionalities. *npj 2D Mater. Appl.* **2**, 18 (2018).
21. Zhou, J. et al. 2DMatPedia, an open computational database of two-dimensional materials from top-down and bottom-up approaches. *Sci. Data* **6**, 86 (2019).
22. Jain, A. et al. Commentary: The Materials Project: a materials genome approach to accelerating materials innovation. *APL Mater.* **1**, 011002 (2013).
23. Li, W. & Li, J. Piezoelectricity in two-dimensional group-III monochalcogenides. *Nano Res.* **8**, 3796–3802 (2015).
24. de Jong, M. et al. Charting the complete elastic properties of inorganic crystalline compounds. *Sci. Data* **2**, 150009 (2015).
25. Smidt, T. E., Mack, S. A., Reyes-Lillo, S. E., Jain, A. & Neaton, J. B. An automatically curated first-principles database of ferroelectrics. *Sci. Data* **7**, 72 (2020).
26. Duerloo, K.-A. N., Ong, M. T. & Reed, E. J. Intrinsic piezoelectricity in two-dimensional materials. *J. Phys. Chem. Lett.* **3**, 2871–2876 (2012).
27. Xu, R., Kim S.-G. Figures of Merits of Piezoelectric Materials in Energy Harvesters. In: *PowerMEMS*) (2012).
28. Roundy, S., Wright, P. K., Rabaey, J. M. *Energy Scavenging for Wireless Sensor Networks: With Special Focus on Vibrations*. Kluwer Academic Publishers (2004).
29. Fei, R., Li, W., Li, J. & Yang, L. Giant piezoelectricity of monolayer group IV monochalcogenides: SnSe, SnS, GeSe, and GeS. *Appl. Phys. Lett.* **107**, 173104 (2015).
30. Dubois, M.-A. & Murali, P. Properties of aluminum nitride thin films for piezoelectric transducers and microwave filter applications. *Appl. Phys. Lett.* **74**, 3032–3034 (1999).
31. Kamel, T. M. et al. Modeling and characterization of MEMS-based piezoelectric harvesting devices. *J. Micromech. Microeng.* **20**, 105023 (2010).
32. Bersuker, I. B. Pseudo-Jahn-Teller effect—a two-state paradigm in formation, deformation, and transformation of molecular systems and solids. *Chem. Rev.* **113**, 1351–1390 (2013).
33. Yao, K. & Tay, F. E. H. Measurement of longitudinal piezoelectric coefficient of thin films by a laser-scanning vibrometer. *IEEE Trans. Ultrason., Ferroelectr., Frequency Control* **50**, 113–116 (2003).
34. Kalinin, S. V., Gruverman, A. *Scanning Probe Microscopy: Electrical and Electromechanical Phenomena at the Nanoscale*. Springer New York (2006).
35. Denning, D., Guyonnet, J. & Rodriguez, B. J. Applications of piezoresponse force microscopy in materials research: from inorganic ferroelectrics to piezoelectrics and beyond. *Int. Mater. Rev.* **61**, 46–70 (2016).
36. Sharma, P. et al. Orientational imaging in polar polymers by piezoresponse force microscopy. *J. Appl. Phys.* **110**, 052010 (2011).
37. Kim, J., You, M., Kim, K.-E., Chu, K. & Yang, C.-H. Artificial creation and separation of a single vortex–antivortex pair in a ferroelectric flatland. *npj Quantum Mater.* **4**, 29 (2019).
38. Borowiak, A. S. et al. Electromechanical response of amorphous LaAlO<sub>3</sub> thin film probed by scanning probe microscopies. *Appl. Phys. Lett.* **105**, 012906 (2014).
39. Bark, C. W. et al. Switchable induced polarization in LaAlO<sub>3</sub>/SrTiO<sub>3</sub> heterostructures. *Nano Lett.* **12**, 1765–1771 (2012).
40. Posternak, M., Resta, R. & Baldereschi, A. Role of covalent bonding in the polarization of perovskite oxides: the case of KNbO<sub>3</sub>. *Phys. Rev. B* **50**, 8911–8914 (1994).
41. You, L. et al. Origin of giant negative piezoelectricity in a layered van der Waals ferroelectric. *Sci. Adv.* **5**, eaav3780 (2019).
42. Zhang, L. et al. Dual-stage nanopositioning scheme for 10 Tbit/in<sup>2</sup> hard disk drives with a shear-mode piezoelectric single-crystal microactuator. *IEEE Trans. Magn.* **51**, 1–9 (2015).
43. Kresse, G. & Furthmüller, J. Efficient iterative schemes for ab initio total-energy calculations using a plane-wave basis set. *Phys. Rev. B* **54**, 11169–11186 (1996).
44. Kresse, G. & Joubert, D. From ultrasoft pseudopotentials to the projector augmented-wave method. *Phys. Rev. B* **59**, 1758–1775 (1999).
45. Perdew, J. P., Burke, K. & Ernzerhof, M. Generalized Gradient Approximation Made Simple. *Phys. Rev. Lett.* **77**, 3865–3868 (1996).
46. Mathew, K. et al. Atomate: A high-level interface to generate, execute, and analyze computational materials science workflows. *Computational Mater. Sci.* **139**, 140–152 (2017).
47. Jain, A. et al. FireWorks: a dynamic workflow system designed for high-throughput applications. *Concurrency Comput.: Pract. Experience* **27**, 5037–5059 (2015).
48. Choudhary, K., Cheon, G., Reed, E. & Tavazza, F. Elastic properties of bulk and low-dimensional materials using van der Waals density functional. *Phys. Rev. B* **98**, 014107 (2018).
49. Wang, H. & Qian, X. Two-dimensional multiferroics in monolayer group IV monochalcogenides. *2D Mater.* **4**, 015042 (2017).

## Acknowledgements

Y.W. acknowledges support from the NUS Research Scholarship. K.Y. and W.H.L. acknowledge partial support from the National Research Foundation, under the Competitive Research Programme of Singapore, NRF-CRP15-2015-04, and A\*STAR, under RIE2020 AME Individual Research Grant (IRG) (Grant No.: A20E5c0086). G.E. acknowledges support from the Singapore MOE (Grant No. MOE2018-T3-1-005). L.S. acknowledges support from the Singapore MOE (Grant Nos. R-265-000-691-114 and MOE2019-T2-2-030, respectively). K.P.L. acknowledges funding from A\*STAR AME-IRG program (Grant No: A1983c0035). Y.W., I.A., I.V., G.E., K.P.L., and S.Y.Q. acknowledge support from the Singapore National Research Foundation, Prime Minister's Office, under its medium-sized center program. Y.W. acknowledges technical help from Miguel Dias Costa and Jun Zhou. Computations were performed on the NUS CA2DM computational cluster and National Supercomputing Centre Singapore. The authors would like to thank Yuan Ping Feng for his comments on the manuscript.

## Author contributions

S.Y.Q. and L.S. conceived the project. S.Y.Q. led the collaborative effort and direction of the project, and provided guidance on the theoretical analysis and calculations. L.S. provided guidance on the high-throughput piezoelectric calculations. Y.W. performed the calculations and theoretical analysis. I.A. designed the experiments and performed micromechanical cleavage, device fabrication, and material characterization under the supervision of K.P.L. K.C.K., L.W., and I.A. performed the PFM measurements. K.C.K. performed the P-E measurements. I.V. synthesized the NbOX<sub>2</sub> bulk crystals under the supervision of G.E. W.H.L performed the LSV measurements under the guidance of K.Y., and both analyzed the results. Y.W., I.A., and S.Y.Q. wrote the manuscript. All authors read and commented on the manuscript.

## Competing interests

The authors declare no competing interests.

**Additional information**

**Supplementary information** The online version contains supplementary material available at <https://doi.org/10.1038/s41467-022-29495-y>.

**Correspondence** and requests for materials should be addressed to Kian Ping Loh, Lei Shen or Su Ying Quek.

**Peer review information** *Nature Communications* thanks the other anonymous reviewer(s) for their contribution to the peer review of this work.

**Reprints and permission information** is available at <http://www.nature.com/reprints>

**Publisher's note** Springer Nature remains neutral with regard to jurisdictional claims in published maps and institutional affiliations.



**Open Access** This article is licensed under a Creative Commons Attribution 4.0 International License, which permits use, sharing, adaptation, distribution and reproduction in any medium or format, as long as you give appropriate credit to the original author(s) and the source, provide a link to the Creative Commons license, and indicate if changes were made. The images or other third party material in this article are included in the article's Creative Commons license, unless indicated otherwise in a credit line to the material. If material is not included in the article's Creative Commons license and your intended use is not permitted by statutory regulation or exceeds the permitted use, you will need to obtain permission directly from the copyright holder. To view a copy of this license, visit <http://creativecommons.org/licenses/by/4.0/>.

© The Author(s) 2022